Astron. Astrophys. 343, 599–607 (1999)

ASTRONOMY AND ASTROPHYSICS

X-ray emission from wind blown interstellar bubbles

II. ROSAT PSPC observations of S 308

M. Wrigge

Hamburger Sternwarte, Gojenbergsweg 112, D-21029 Hamburg, Germany

Received 10 March 1997 / Accepted 16 November 1998

Abstract. We have obtained ROSAT observations of several wind blown interstellar bubbles. In this paper we present the results of the PSPC observations of S 308 which optically shows a spherically symmetric shell with only slight hints on developing instabilities. It should therefore be a prototypical object for 1d and spherical 2d models. The X-ray surface brightness is very low. We have determined a total luminosity of $L_{\rm x} \approx 3.7\ 10^{33}\ {\rm erg\,s^{-1}}$ and plasma temperatures in the range $T = (1.5 \ldots 28)\ 10^6$ K. The emitting volume is a thick shell with a ratio of inner to outer radius of ≈ 0.5. Both $L_{\rm x}$ and the observed count rate surface profiles do not compare very well with predictions from current models. Also, the observed wind power is two orders of magnitude greater than needed as input by the models to produce the observed bubble. This stellar wind strength problem is similar to the one García-Segura and MacLow found in their numerical models for NGC 6888.

Key words: X-rays: ISM – ISM: individual objects: S 308 – ISM: bubbles – stars: Wolf-Rayet – stars: individual: EZ CMa

1. Introduction

The interaction of strong stellar winds with the medium ambient to the star can produce large ($\approx 10\ {\rm pc}$) cavities around the star filled with a hot ($\approx 10^6$ K) tenuous ($\approx 10^{-3}\ {\rm cm^{-3}}$) X-ray emitting gas, so called wind driven interstellar bubbles.

One would expect wind driven bubbles around most stars with supersonic winds and high mass loss rates. The most promising candidates then are Wolf-Rayet and Of stars with typical mass loss rates of a few $10^{-5}\ {\rm M_\odot\,yr^{-1}}$ and wind terminal velocities v_∞ of around $2000\ {\rm km\,s^{-1}}$ (van der Hucht, 1992 and references therein) thus yielding wind luminosities $L_w = \frac{1}{2}\dot{M}{v_\infty}^2$ of the order $10^{38}\ {\rm erg\,s^{-1}}$. But in contrast to what is expected only a few WR stars do actually have wind blown bubbles.

From the recent candidate lists from Chu et al. (1983), Heckathorn et al. (1982), Miller & Chu (1993) and Marston et al. (1994) about $1/4$ to $1/3$ of all observed galactic WR stars seem to be associated with ring nebulae, but from these only a very small number of about 10 remain as wind driven bubbles according to the classification scheme based on optically derived kinematics of the shell (Chu, 1981). The observations thus suggest that the models put forward so far are not complete (see Wrigge et al. 1994, hereafter Paper I).

In Weaver et al.'s (1977) model the supersonic wind expands into a homogenous medium. García-Segura & MacLow (1995a) recently suggested a $\rho \propto r^{-2}$ density profile for the ambient medium. In fact according to the evolutionary sequence of massive stars (for a review see Chiosi & Maeder, 1986, also van der Hucht, 1992, Langer et al. 1994) the progenitor of a WR star is a luminous blue variable ($M \geq 60\ {\rm M_\odot}$) or a red supergiant (RSG) ($25\ {\rm M_\odot} \leq M \leq 60\ {\rm M_\odot}$). In the latter case the fast WR wind will expand into the slow RSG wind with a density $\rho \propto r^{-2}$ which naturally results in Rayleigh-Taylor instabilities in the outer shock front. In 2d hydrodynamical simulations García-Segura & MacLow (1995b) demonstrated the development of instabilities showing a remarkable resemblance with optical observations of the prototypical object NGC 6888, but it was not possible to predict the observed X-ray flux *and* X-ray morphology (see Paper I) when inserting the observed wind power L_w (García-Segura & MacLow, 1995a, hereafter GM). This might be due to the effects of evaporation and heat conduction of the warm filaments embedded in the hot interior plasma of the bubble.

In this second paper of a series we report on our ROSAT X-ray observations of the wind driven bubble S 308 around the WN5 star EZ CMa (= HD 50896 = WR 6[1]). In optical images the nebula appears nearly circular without readily discernible shell instabilities. Assuming that there are indeed no clumps embedded in the hot plasma S 308 should be a better protoype for dynamically young wind driven bubbles than NGC 6888. Spherically symmetric analytical calculations should describe the dynamics well and numerical simulations should not have to cope with heat conduction and evaporation of irregulary shaped cloudlets of various scales. The observed total X-ray luminosity and surface brightness distribution set strong constrains on the modelling of bubbles.

2. Observations and data reduction

The ring nebula S 308 centered on the Wolf-Rayet star EZ CMa was observed with the ROSAT PSPC detector in two observing runs. (For a general description of ROSAT see Trümper, 1983.

Send offprint requests to: M. Wrigge (mwrigge@hs.uni-hamburg.de)

[1] WR number from van der Hucht et al. (1981)

A description of the ROSAT PSPC is given by Pfeffermann et al. , 1986.) The first originally proposed by our group was conducted during AO1 in April 1991 with a total exposure time of 5865 sec. The second observation aiming at the X-ray emission of the central WR star was proposed for AO3 by Willis and performed in March 1992 with a total exposure time of 9128 sec. To enhance the signal to noise ratio of the X-ray image we obtained Willis' observation from the MPE archive and merged both data sets using the appropriate EXSAS routines (see Zimmermann et al. 1994).

From Weaver et al.'s (1977) theory of wind blown bubbles one expected a filled bubble morphology with quite a flat X-ray surface brightness distribution with a moderate limb-brightening. Consequently our observations of S 308 were centered on the WR star. This proved to be unfortunate in hindsight since from our analysis of the X-ray emission of NGC 6888 (Paper I) the highest X-ray surface brightness is now to be expected in a thin shell following the inner edge of the optically visible nebula emission. In the case of S 308 the optical circular shell has a diameter of $40'$ which happens to be the same as the diameter of the inner ring of the support structure of the PSPC entrance window. Thus a certain amount of the diffuse emission of the bubble might be screened off by the support ring hampering the analysis of the spatial structure of the diffuse emission.

A further serious problem in analyzing the X-ray observations of S 308 is the large size of the nebula. The background emission has to be defined using areas far outside the inner detector ring where the effective area of the detector drops by a factor of 1.5 at an off axis angle of $40'$ compared to the on-axis value. Furthermore care has to be taken when removing any non vignetted background contributions, namely after-pulses and particle events, and when accounting for the spatially not uniform background of scattered solar X-rays.

Similar to the prescription given by Snowden et al. (1994) we inspected the background spectrum (excluding all point sources) for indications of after-pulses in the lowest pulse height channels and found that there seems to be no contamination. The same is true for the scattered solar X-rays after inspecting the background light curves. To minimize the contribution of particle events we only used observation times where the transmitted master veto rate was less than $150\ \mathrm{s}^{-1}$. This leads to an effective exposure time of 13434 sec for the merged dataset. From the veto rate time series we estimated a mean veto rate of $78\,\mathrm{s}^{-1}$ and using the particle background parameterization of Plucinsky et al. (1993) for the high gain state of the detector (valid for the first observing period of S 308) we find a background count rate due to particle events of $0.13\,\mathrm{s}^{-1}$. This corresponds to a surface brightness of $1.2\ 10^{-5}\,\mathrm{s}^{-1}\,\mathrm{arcmin}^{-2}$ which is subtracted from the X-ray images before vignetting correction.

For correcting the images for the angular and energy dependent effective exposure time we created X-ray images in those PSPC bands for which detector maps exist. These images were then divided by effective exposure maps constructed for each of the bandpasses from the detector maps using EXSAS routines. The detector maps used are those delivered with the EXSAS JAN 94 software package. Since the second observations were performed in the low gain state of the PSPC one should not use channels 8–10. Since there are no detector maps available within the EXSAS distribution for channels 11–19 we used the corresponding map provided by HEASARC at Goddard Space Flight Center. For correcting the X-ray image of the total band we used the mean of the detector maps for creating the total exposure map.

3. The diffuse X-ray emission from S 308

The only pre-ROSAT X-ray observations of S 308 were those by the *Einstein* X-ray Observatory. No extended diffuse X-ray emission was detected above a surface brightness (3σ level) of $3.7\ 10^{-4}\ \mathrm{s}^{-1}\,\mathrm{arcmin}^{-2}$.

3.1. A map of the diffuse emission

Fig. 1 shows the flatfielded PSPC image in the energy range from 0.1 keV to 2.04 keV as a contour plot superimposed onto the grey scale [OIII] image obtained by Chu et al. (1982). To enhance the contrast of the diffuse emission without degrading the spatial resolution too much the original image with $15''$ pixelsize and a nominal on-axis angular resolution of about $30''$ was smoothed with a Gaussian filter of $63''$ FWHM resulting in an image with the same pixelsize and an angular resolution of $70''$.

Fig. 2 shows the same X-ray image as greyscale with the effective exposure time superimposed as a contour plot. This depicts the position of the inner ring and the support struts of the entrance window. Though lying close to the window support structure extended diffuse emission is well discernible in the northwestern parts of the shell. The surface brightness in the bright parts of these filaments is typically about $3\,10^{-3}\,\mathrm{s}^{-1}\,\mathrm{arcmin}^{-2}$ with a maximum of $6.5\ 10^{-3}\ \mathrm{s}^{-1}\,\mathrm{arcmin}^{-2}$ in the blow out region. The background surface brightness is $(1.0 \pm 0.3)\ 10^{-3}\ \mathrm{s}^{-1}\,\mathrm{arcmin}^{-2}$ where the standard deviation is the square root of the mean quadratic point to point deviation of the surface brightness in the image. From the image there is no excess emission visible to the eye in the inner $40'$ of the field of view on the first sight.

3.2. Radial and angular distribution of diffuse emission

As the optical shell is more or less spherically symmetric the same might be assumed for the interior X-ray emission. To further investigate its radial distribution we integrated the surface brightness over ring sectors with constant width and 90° intervalls in azimuth. These calculations were performed on the flatfielded total band image with the exception of circular areas around the visible point sources and the support structure. Fig. 3 shows the surface brightness as a function of ring radius for the annotated azimuth angle intervals. The upper four panels show the variation of the radial surface brightness distribution between 90° intervalls. Clearly the angular distribution is not spherically symmetric. Instead we find the maximum emission

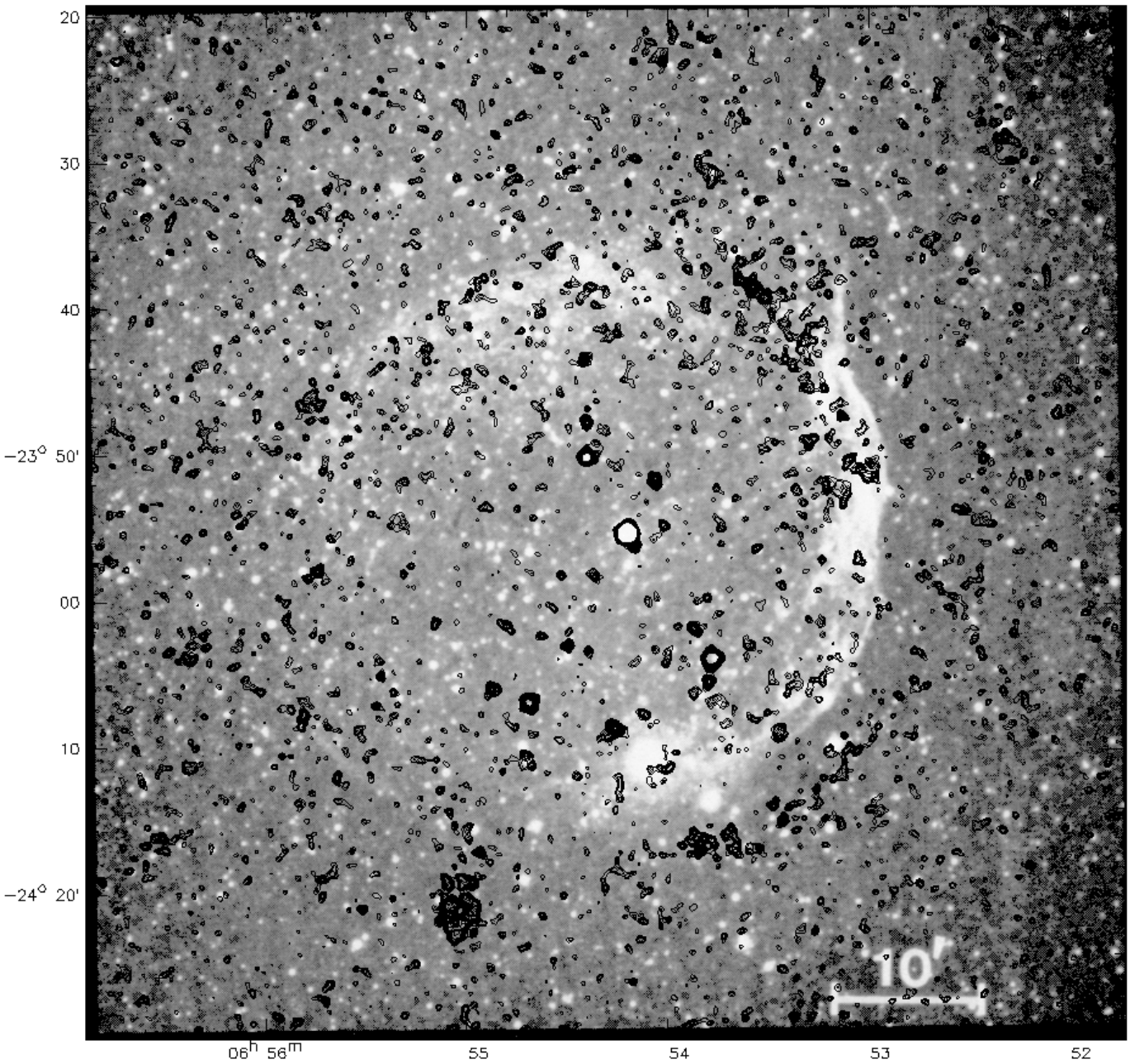

Fig. 1. X-ray contour plot superimposed on a greyscale [OIII] image originally obtained by Chu et al. (1982). The contour levels are from $3\,\sigma$ above the background of $1.0\,10^{-3}\,\mathrm{cts\,s^{-1}\,arcmin^{-2}}$ with $0.3\,10^{-3}\,\mathrm{cts\,s^{-1}\,arcmin^{-2}}$ $(1\,\sigma)$ stepwidth. The image is convolved to a resolution of $70''$. Clearly visible are the central WR star, the [OIII] ring and the blow out region (both in [OIII] and X-ray). Coordinates are J2000.

in the northwestern area of the nebula (angle $270°$ to $360°$) as is already discernible in Figs. 1 and 2. This region coincides with a [OIII] blow out. In contrast there is no excess emission above the background in the southeastern parts of the nebula (position angle $90°$ to $180°$). Note that the background is flat over the whole field of view.

The bottom left panel for the surface brightness integrated from $0°$ to $360°$ evidently shows an excess emission originating in a ring with an inner radius of $12'$ and an outer radius of $25'$ measured at half maximum points; the radii correspond to $7\ \mathrm{pc}$ and $14.5\ \mathrm{pc}$ at a distance of $2\ \mathrm{kpc}$. This translates into the geometry of a thick shell with a ratio of inner to outer radius of ≈ 0.5. What fraction of the apparent emission between $25'$ and $30'$ is real remains to be seen in observations with higher sensitivity. The maximum surface brightness is about $0.3\,10^{-3}\,\mathrm{s^{-1}\,arcmin^{-2}}$ above background. Integrating over the whole nebula, i.e. over all pixels with excess emission, gives a total observed count rate of $0.34\,\mathrm{s^{-1}}$ (excluding channels 8–10, see above).

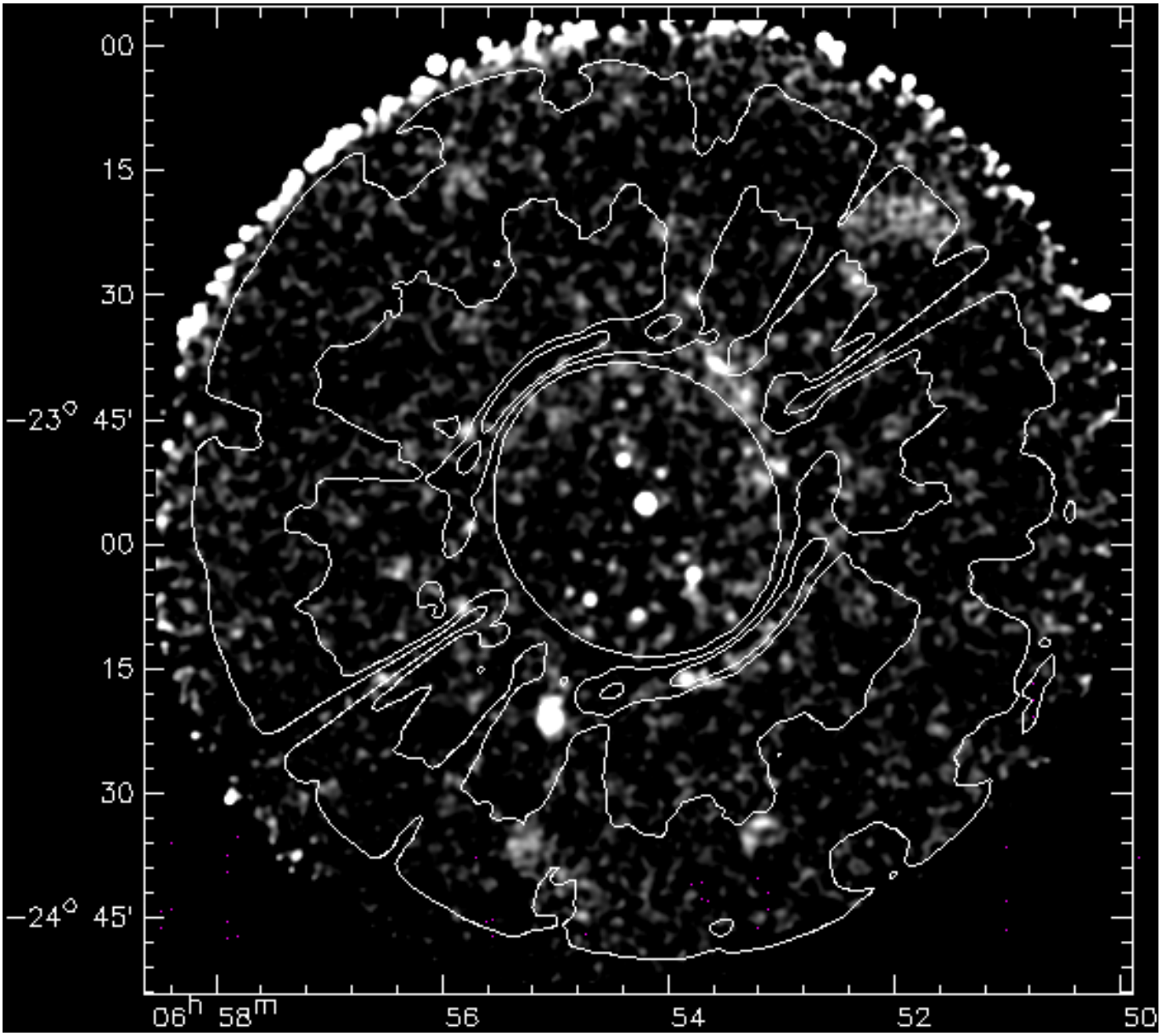

Fig. 2. The greyscale shows the vignetting corrected total band PSPC image convolved to a resolution of 70″. The range is from $1.1\ 10^{-3}$ to $2.6\ 10^{-3}$ $\mathrm{cts\,s^{-1}\,arcmin^{-2}}$. Coordinates are J2000. The overlay shows the effective exposure time as a contour plot with contour lines every 2000 sec starting at 7000 sec. Clearly visible are the inner ring and the ribs of the entrance window support structure in the contour plot. The grey scale image shows a number of point sources including the central WR star. Note also the diffuse filament in the northwestern area near the window support ring. The conspicous bright dots circling the upper part of the image are numerical artifacts due to the vignetting correction when dividing with the exposure map.

3.3. A X-ray spectrum of the diffuse emission

With a count rate of $0.34\ \mathrm{s^{-1}}$ we expect a total number of 4560 net source photons in 13434 sec life time which should yield a spectrum with high signal to noise ratio suitable for spectral analysis. Usually we used EXSAS routines for extracting source and background spectra which where properly normalized to on-axis effective area and subtracted. This procedure had difficulties when dealing with large source and background areas and with large off-axis angles. Especially the fact that the ring of the window support structure lies within regions of interest forced us to use another procedure. We calculated a net source count rate directly from the radial profiles for each of the seven bands for which we created vignetting corrected images (see above). In all cases we took $r = 30'$ as the outer radius of the possible diffuse emission. We then determined the background count rates in each band from the background surface brightness outside the source area (Fig. 3). This resulted in spectra with 7 spectral bins with high signal-to-noise (Fig. 4); note that the PSPC's spectral resolution equals four independent spectral bands.

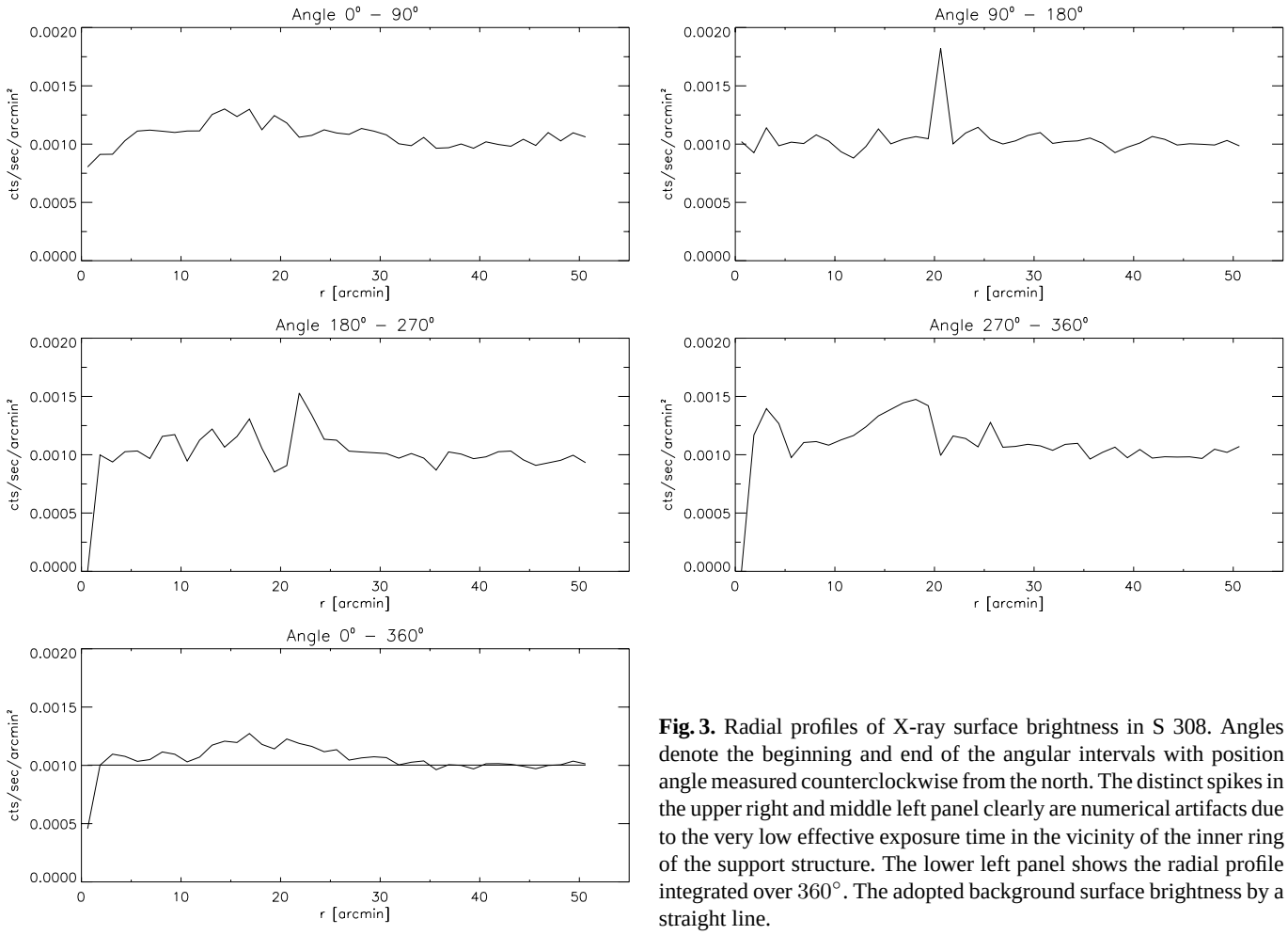

Fig. 3. Radial profiles of X-ray surface brightness in S 308. Angles denote the beginning and end of the angular intervals with position angle measured counterclockwise from the north. The distinct spikes in the upper right and middle left panel clearly are numerical artifacts due to the very low effective exposure time in the vicinity of the inner ring of the support structure. The lower left panel shows the radial profile integrated over 360°. The adopted background surface brightness by a straight line.

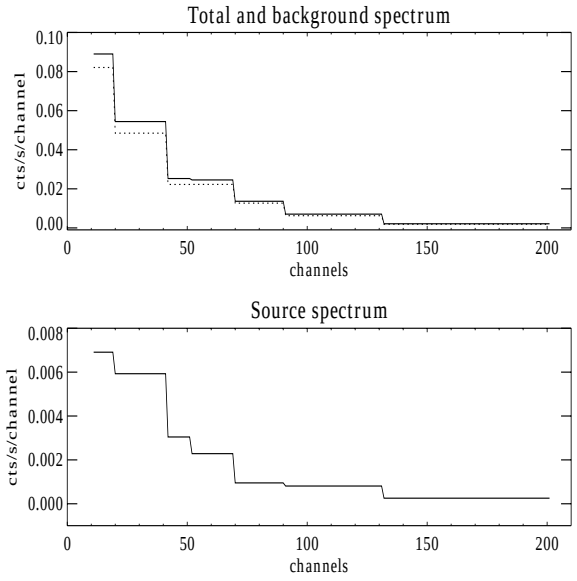

Fig. 4. Pulse height spectrum of the diffuse emission from S 308

This procedure was tested against the previously published results on NGC 6888 (Paper I) and resulted in the same count rate spectrum and derived fit parameters as obtained with the EXSAS routines. Since thermal plasma emission seems to be the only reasonable mechanism, we fitted a model according to Raymond & Smith (1977) to the data. To further reduce the number of free parameters the column density of neutral hydrogen was set to a fixed value. Schmutz & Vacca (1991) found a reddening of $E_{\rm B-V} = 0.06$ towards EZ CMa which translates into $N_{\rm H} = 3.5\ 10^{20}\ {\rm cm}^{-2}$ ($N_{\rm H} = 5.8\ 10^{21}\ E_{\rm B-V}\ {\rm cm}^{-2}$, Bohlin et al., 1978). Actually EZ CMa was in the original sample of stars observed with the *Copernicus* sattelite to derive the $N_{\rm H} - E_{\rm B-V}$ relation. Bohlin et al. found $N_{\rm H} = 3.5\ 10^{20}\ {\rm cm}^{-2}$ with an uncertainty of 30%. Shull & van Steenberg (1985) observed EZ CMa with IUE and derived essentially the same values. Finally, Willis & Stevens (1996) found $N_{\rm H} \approx 4\ 10^{20}\ {\rm cm}^{-2}$ from their black-body fits to the ROSAT PSPC count rate spectrum of EZ CMa. We thus used a fixed $N_{\rm H} = 3.5\ 10^{20}\ {\rm cm}^{-2}$. Note that the observed spectrum of the diffuse emission is indeed very soft compared to NGC 6888 due to the lower column density of absorbing foreground interstellar matter.

Our first trials with a one temperature RS plasma resulted in spectra with low temperature of about $1.6\ 10^6$ K which reproduced well the low energy region but deviated so strongly from the observed count rates at energies above 0.5 keV that

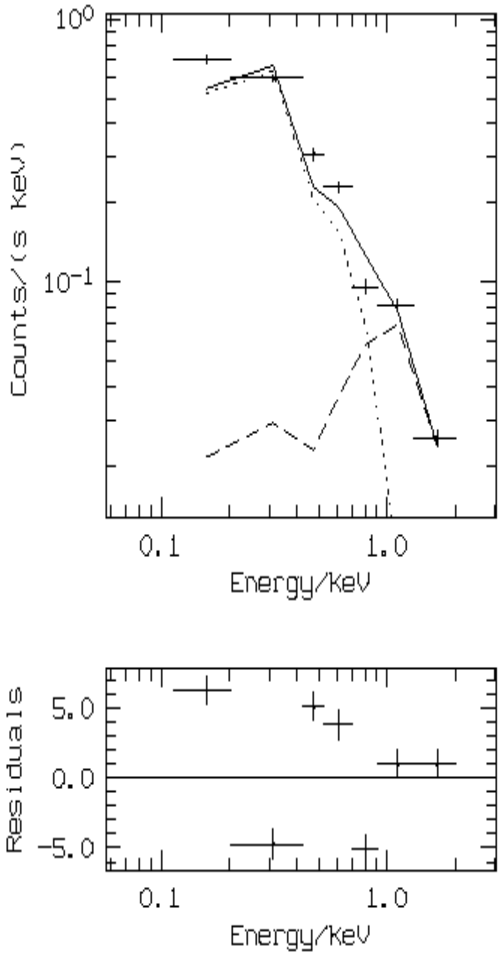

Fig. 5. Fit of Raymond & Smith thermal plasma emission to the observed count rate spectrum of S 308. The dotted and dashed curves show the low and high temperature component, respectively.

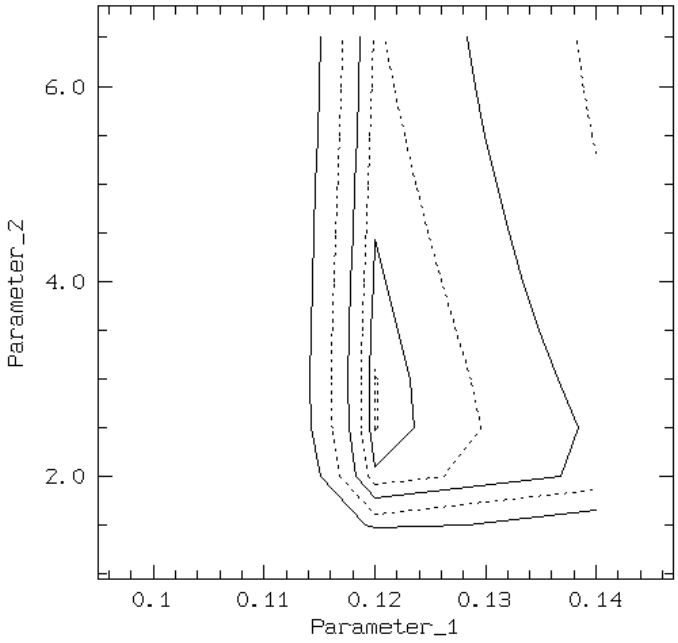

Fig. 6. χ^2 contour plot corresponding to the fit shown in Fig. 5. Parameter 1 and 2 are the lower and higher temperatures measured in keV (1 keV $= 1.16\ 10^7$ K), respectively. Contours are in steps of $1\,\sigma$

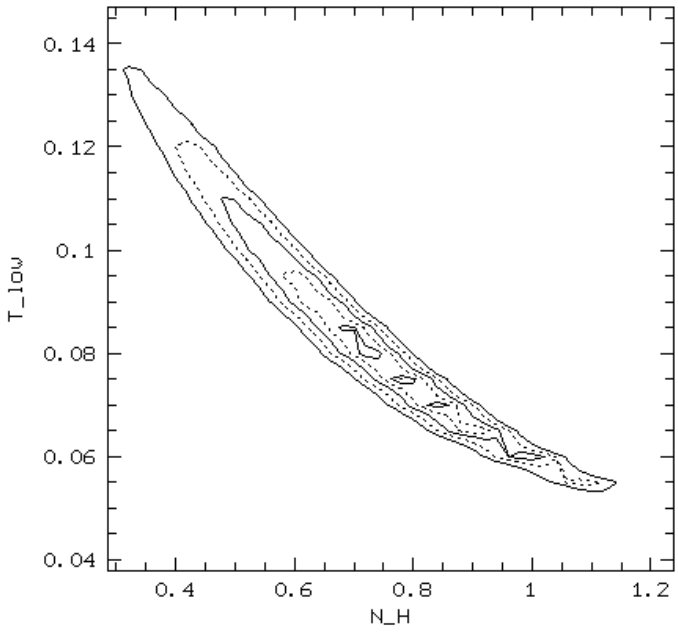

Fig. 7. χ^2 contour plot corresponding to the fit shown in Fig. 5. The parameters are the lower temperatures measured in keV (1 keV $= 1.16\ 10^7$ K) and the hydrogen column density $N_{\rm H}$ in $10^{21}\ {\rm cm}^{-2}$. Contours are in steps of $1\,\sigma$

an isothermal plasma can be excluded. Though only seven data points are present we tried a two temperature fit shown in Fig. 5. Fig. 6 shows the χ^2 grid of the fit with both temperatures as fixed parameters, Fig. 7 shows the χ^2 grid of the lower temperature against $N_{\rm H}$. The resulting two components have temperatures of $(1.5 \pm 0.1)\ 10^6$ K and $(2.8 \pm 0.4)\ 10^7$ K with flux normalization constants $A = (2.6 \pm 0.4)\ 10^{11}\ {\rm cm}^{-5}$ and $A = (1.1 \pm 0.3)\ 10^{11}\ {\rm cm}^{-5}$, respectively, where $A = 1/(4\,\pi\,D^2)\ \int {n_e}^2\,dV$. The fit has a χ^2 of ≈ 40 which clearly shows that the plasma emission can not be described by a two component RS plasma either. Since we actually do not expect the bubble to be isothermal the numbers should be regarded as an estimate of the prevailing temperature range. Especially the higher temperature may be regarded as a sort of a maximum existing temperature. From the spectral fit we find an observed X-ray flux of $2.7\ 10^{-12}\ {\rm erg\,cm^{-2}\,s^{-1}}$ which in spite of the bad fit should be realistic for the order of magnitude.

In order to highlight the importance of a temperature range we calculate the intrinsic absorption corrected fluxes and luminosities for each of the two temperature components but using conversion factors for converting count rates to intrinsic fluxes for the appropriate temperatures (Table 1). We adopted a distance of $2\ {\rm kpc}$ though the true distance might be in the range $1 \ldots 2\ {\rm kpc}$ (Hamann et al. 1988) and $N_{\rm H} = 3.5\ 10^{20}\ {\rm cm}^{-2}$ (see above). This is well compatible with the results of Howarth & Schmutz (1995) who find $D = 1.8\ {\rm kpc}$ with an estimated uncertainty of 15%. Dividing the total observed count rate be-

Table 1. Unabsorbed fluxes, luminosities, and count rate to flux conversion factors, for different plasma temperatures. The total band count rate is $0.34\ \mathrm{s}^{-1}$

	$T = 1.5\ 10^6$ [K]	$T = 2.8\ 10^7$ [K]
$f_{\mathrm{X,unabs}}$ [erg cm^{-2} s^{-1}]	$9.2\ 10^{-12}$	$5.2\ 10^{-12}$
L_{X} [erg s^{-1}]	$4.4\ 10^{33}$	$2.5\ 10^{33}$
cf [erg cm^{-2} cts^{-1}]	$2.7\ 10^{-11}$	$1.5\ 10^{-11}$

tween the two phases according to their respective emission measures yields a total intrinsic flux of $6.5\ 10^{-12}\ \mathrm{erg\,cm^{-2}\,s^{-1}}$ and $1.2\ 10^{-12}\ \mathrm{erg\,cm^{-2}\,s^{-1}}$ for the cooler and hotter gas, respectively, resulting in a luminosity of $L_{\mathrm{X}} = 3.7\ 10^{33}\ \mathrm{erg\,s^{-1}}$. Thus having such a low temperature plasma the X-ray luminosity is much more dependent on the assumed absorption than on trying to fix a temperature value. Conversion factors are calculated for a range of N_{H} and temperatures (Table 2). The absorption corrected flux more than doubles for the low temperature component with twice the assumed N_{H} and increases by a factor of 4.4 for $N_{\mathrm{H}} = 9\ 10^{20}\ \mathrm{cm^{-2}}$. The conversion factor for the high temperature component remains essentially constant. As the column density of interstellar hydrogen is reasonably fixed by independent observations (see discussion above) the second line in Table 2 should represent the possible order of magnitude for the X-ray luminosity. For the following discussion we adopt the above luminosity value.

4. Discussion

We now compare the derived X-ray luminosity with the predictions from the analytical models of Weaver et al. (1977) and GM. We first summarize the input parameters. Hamann et al. (1993) found from their models of WR atmospheres that the most probable consistent set of wind parameters are a stellar mass loss rate of $\log(\dot{M}[\mathrm{M_\odot\,yr^{-1}}]) = -4.1$, a terminal wind velocity of $v_\infty = 1700\ \mathrm{km\,s^{-1}}$ and a stellar distance of $D = 2$ kpc. It should be noted that a mass loss rate of $\log(\dot{M}\,[\mathrm{M_\odot\,yr^{-1}}]) = -4.4$ and a distance of D $= 1.1$ kpc are also compatible with the models (Hamann et al. 1988) but a distance of 2 kpc is generally preferred. The stellar wind terminal velociy derived from optical spectroscopy given above certainly is a lower limit since UV measurements yield $v_\infty = 2500\ \mathrm{km\,s^{-1}}$ (Willis, 1982).

Identifying the outer nebula shell visible in the optical with the outer shock front the linear diameter of the nebula is about 23 pc. Chu et al. (1982) found an expansion velocity of $60\ \mathrm{km\,s^{-1}}$. They derived a shell mass of $40\ \mathrm{M_\odot}$ of ionized material at a distance of 1.5 kpc using the radio observations by Johnson (1971) and assuming the shell is swept up interstellar material. In their equations the shell mass scales with $D^{2.5}$ thus resulting in $M_{\mathrm{shell}} \approx 82\ \mathrm{M_\odot}$ for our preferred distance (see Table 3). With these parameters GM's analytical model predicts a X-ray luminosity of $9\ 10^{33}\ \mathrm{erg\,s^{-1}}$ in the ROSAT band which is comparable with the observed value of $3.7\ 10^{33}\ \mathrm{erg\,s^{-1}}$ considering the uncertainty in the determination of the observed L_{x} and the parameters entering the analytical calculation. But the wind luminosity producing the bubble according to this model should be $L_w \approx 1.5\ 10^{36}\ \mathrm{erg\,s^{-1}}$ whereas the actual luminosity of EZ CMa's wind is $7\ 10^{37}\ \mathrm{erg\,s^{-1}}$ which is larger by a factor of 46! Note that the wind luminosity enters GM's calculations of L_x as $L_w^{13/21}$.

We have also calculated the expected X-ray flux from S 308 in the ROSAT PSPC band numerically. Using the analytical temperature and density profile (see Fig. 8) and emissivities according to the Raymond & Smith model with a lower temperature threshold of $1\ 10^5$ K, we find an expected L_{x} of $1.4\ 10^{35}\ \mathrm{erg\,s^{-1}}$! This dramatic difference of nearly a factor of 30 to GM's own analytical calculation of L_{x} is due to the fact that they used $T_{\mathrm{low}} = 5\ 10^5$ K as their lower threshold for the X-ray emissivity, but in fact a large amount of flux originates near the outer edge where the density is high but the temperature is low. Even if we tune N_{H} and T_{low} to values resulting in an observed L_{x} of around $10^{35}\ \mathrm{erg\,s^{-1}}$ compatible with the model (namely $N_{\mathrm{H}} \sim 8\ 10^{20},\ T_{\mathrm{low}} \sim 9\ 10^5$) but unplausible compared to other observational facts (N_{H}) the modelled wind luminosity would still be a factor of ~ 50 smaller than the actually observed L_{w}. Thus since L_w and L_x do not have consistent values within the framework of GM's model one might argue that S 308 is not represented by the two-wind model.

Instead, S 308 might be a classical wind blown bubble a lá Weaver et al. (1977), i.e. the ambient medium has constant density. In fact in the framework of the classical bubble the wind luminosity necessary to create a shell with radius R_{shell} is

$$L_{\mathrm{w}} = (308\pi/250)\,\rho_0\,t_{\mathrm{dyn}}^{-3}\,{R_{\mathrm{shell}}}^5$$

with an ambient density ρ_0. With $R_{\mathrm{shell}} = 11$ pc and $v_{\mathrm{exp}} = 60\ \mathrm{km\,s^{-1}}$ (Chu et al. 1982) the dynamical age is $t_{\mathrm{dyn}} = \eta\,R_{\mathrm{shell}}/v_{\mathrm{exp}} = 113000$ yr with $\eta = 0.6$ (energy conserving bubble, see Weaver et al. 1977). The wind luminosity neccessary to produce the bubble then is $L_{\mathrm{w}} \approx 8\ 10^{36}\ n_0$. This would imply an ambient ISM particle density of $25\ \mathrm{cm^{-3}}$ which seems very unreasonable for an object 350 pc (190 pc for the smaller distance) below the galactic plane. In fact, a bubble volume of $\approx 2\ 10^{59}\ \mathrm{cm^{-3}}$ and a shell mass of $82\ \mathrm{M_\odot}$ require $n_0 \approx 0.5\ \mathrm{cm^{-3}}$ for the ambient density. Thus S 308 can not be described by either Weaver et al.'s or GM's model.

Besides the integral parameter L_{x} we can also calculate the expected count rate surface brightness profile of the bubble. Note that the angular and energy depencies of the ROSAT PSPC have been taken into account. Fig. 9 shows the unabsorbed surface brightness and the expected count rate surface brightness profiles for GM's model with the shell parameters as in Table 3 and a foreground column density of $N_{\mathrm{H}} = 4\ 10^{20}\ \mathrm{cm^{-2}}$ and $N_{\mathrm{H}} = 8\ 10^{20}\ \mathrm{cm^{-2}}$, respectively. Besides the fact that the expected surface brightness is far higher than the observed one, we would expect a more or less centrally filled appearance of S 308 with a marked decrease in brightness towards the limb of the bubble (This is mainly due to the fact, that the low temperature emission originating near the outer shock is far stronger absorbed by the foreground interstellar matter than the emission

Table 2. Conversion factors for count rate to absorption corrected flux $[\mathrm{erg\,cm^{-2}}]$

N_H 10^{20} cm^{-2}	$T = 5.0\,10^5$ [K]	$T = 1.0\,10^6$ [K]	$T = 1.5\,10^6$ [K]	$T = 2.8\,10^7$ [K]
2	$1.3\,10^{-10}$	$2.2\,10^{-11}$	$1.4\,10^{-11}$	$1.3\,10^{-11}$
3.5	$4.7\,10^{-10}$	$5.7\,10^{-11}$	$2.7\,10^{-11}$	$1.5\,10^{-11}$
4	$6.8\,10^{-10}$	$7.5\,10^{-11}$	$3.3\,10^{-11}$	$1.6\,10^{-11}$
6	$2.4\,10^{-9}$	$1.9\,10^{-10}$	$6.3\,10^{-11}$	$1.8\,10^{-11}$
9	$1.2\,10^{-8}$	$5.4\,10^{-10}$	$11.9\,10^{-11}$	$2.0\,10^{-11}$

Table 3. Shell parameters and observed and predicted X-ray and wind luminosities of the diffuse emission in S 308. The index GM refers to García-Segura & MacLow (1995a), WMCSM to Weaver et al. (1977).

	$D = 1.1$ kpc	$D = 2$ kpc
R_shell [pc]	6.4	11.6
V_exp[km s^{-1}]	60	60
V_∞[km s^{-1}]	1700	1700
M_shell [M$_\odot$]	18	82
log($\dot{M}$) M$_\odot$ yr^{-1}	-4.4	-4.0
$L_\mathrm{w,observed}$ [erg s^{-1}]	$4\,10^{37}$	$7.4\,10^{37}$
$L_\mathrm{x,observed}$ [erg s^{-1}]	$1.1\,10^{33}$	$3.7\,10^{33}$
$L_\mathrm{w,GM}$ [erg s^{-1}]	$6\,10^{35}$	$1.5\,10^{36}$
$L_\mathrm{x,GM}$ [erg s^{-1}]	$7.7\,10^{34}$	$1.4\,10^{35}$
$L_\mathrm{w,WMCSM}$ [erg s^{-1}]	$2.4\,10^{36}\,n_0$	$8\,10^{36}\,n_0$
$L_\mathrm{x,WMCSM}$ [erg s^{-1}]	$5\,10^{34}\,{n_0}^{18/35}$	$1\,10^{35}\,{n_0}^{18/35}$

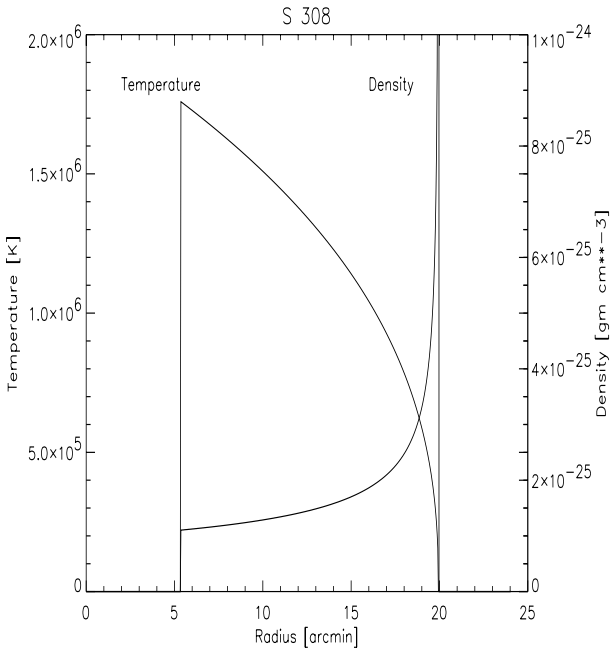

Fig. 8. Temperature and density profile of the wind blown bubble S 308 according to GM's model using the shell parameters given in Table 3

of the hot interior of the bubble. See Fig. 8.) Instead we find a hole in the inner regions of S308.

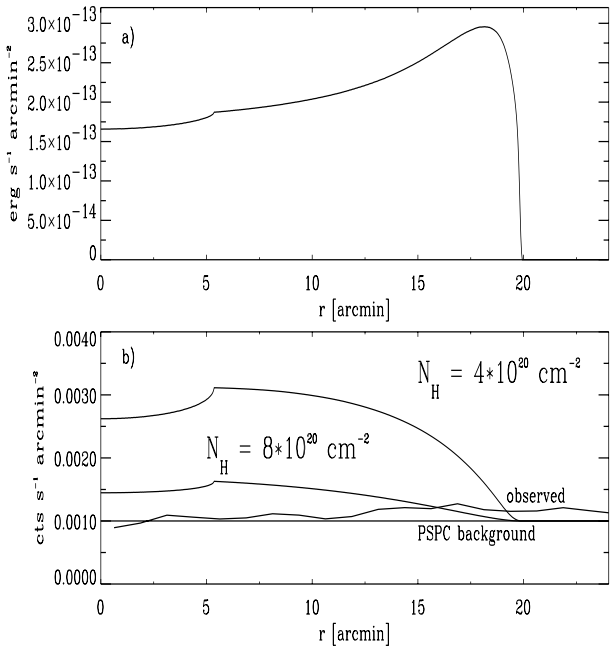

Fig. 9a and b. Expected unabsorbed surface brightness **a** and count rate surface brightness **b** of S 308 according to the model from Garćia-Segura & MacLow (1995a). We used the shell parameters as in Table 3

For the above calculations we have used the radius of the optically visible nebula of 20′ as the so called outer radius of the shell as also adopted by GM. The extension beyond this value as seen in Fig. 3 is dominated by the emission in the area of the northwestern blowout. Thus a choice of a larger outer shell is not compelling. In addition the general conclusions are not altered in such a case.

We will further discuss the total energy budget of the bubble. With a shell mass of $82\,\mathrm{M_\odot}$ and $v_\mathrm{exp} = 60\,\mathrm{km\,s^{-1}}$ the total kinetic energy of the shell is $E_\mathrm{kin,shell} \approx 3\,10^{48}$ erg. From Fig. 3 the radius of the X-ray emitting region can be estimated to be $32'$ corresponding to a volume of $V = 8\,10^{59}\,\mathrm{cm^3}$. Assuming a homogenous spherical bubble with particle density n_int the internal (i. e. thermal) energy is $E_\mathrm{therm} = 3/2\,k\,T\,V\,n_\mathrm{int}$. The internal density can be estimated with ${n_\mathrm{int}}^2 = L_\mathrm{X}/(V\,\Lambda)$ where Λ is the cooling function estimated to be $\Lambda \approx 3\,10^{-23}\,\mathrm{erg\,cm^3\,s^{-1}}$ assuming optically thin equilibrium thermal plasma emission (Raymond & Smith, 1977) at an average temperature of 10^7 K. We thus find $E_\mathrm{therm} = 3/2\,k\,T\,\sqrt{(L_x\,V)/\Lambda} \approx 2.4\,10^{49}$ erg. As we know from NGC 6888 (Paper I) and also can be seen from Fig. 3 the X-ray emission originates in a volume consider-

ably smaller than the volume of the spherical bubble. Therefore $n_{\rm int} \approx 1\,10^{-2}$ cm^{-3} certainly is a lower limit. With a wind luminosity of $L_{\rm w} \approx 7\ 10^{37}$ erg s^{-1} and a dynamical age of 113000 years the stellar wind deposited $E_{\rm w} \approx 3\ 10^{50}$ erg in the ambient medium. This is more than an order of magnitude larger than the amount of energy accounted for by observations (kinetic energy of the shell, thermal energy of the bubble, X-ray radiated energy). This conclusion still holds even considering the poorly determined temperatures allowing for a range of $5\,10^5 \ldots 3\,10^7$ K. Actually $E_{\rm therm}$ decreases with decreasing T in this temperature range. $E_{\rm therm}$ does increase for $T < 5\,10^5$ K but as we argued above, such low temperatures seem to be not plausible at least for most of the bubble volume. (If the temperatures where so low for most of the bubble, a density of $\approx 9\,{\rm cm}^{-3}$ would be needed to account for the observed $L_{\rm x}$, which is only expected in the very periphery of the bubble.)

5. Summary and conclusions

It seems evident that the physical description of the bubble phenomenon is incomplete. Observationally we can only account for less than 10% of the wind energy and thus need a – or a few – mechanisms that allow most of the wind energy to escape observations. In the case of S 308 the proposed 'leaking box' (Lozinskaya, 1992 and references therein) will not work, since the [OIII] bubble is a closed shell (Chu, 1982 and unpublished results) except if there is some strange morphology along the line of sight. A further point is that we might have overestimated the amount of energy deposited in the ambient medium when negelecting the actual mass loss history of the WR star. The discussion above also shows that the recently proposed model which includes the mass loss history can reproduce the dynamics and morphology of the outer shell strikingly well (see García-Segura & MacLow, 1995b for an example) but shows deficiencies when calculating the X-ray luminosity $L_{\rm x}$ and observed count rate surface profiles. When inserting the measured $M_{\rm shell}$ and $v_{\rm exp}$ the calculated $L_{\rm x}$ is two orders of magnitude too large, whereas the calculated wind power $L_{\rm w}$ is a factor of 10 smaller than the observed value (the 'missing wind problem'). The discrepancy between model and observations becomes even more evident when comparing the expected and observed count rate surface brightness profiles. The expected profile is centrally filled, regardless of the foreground column density (within acceptable ranges), wheras the observed surface brightness increases towards the periphery of the nebula. Our ASCA observations of NGC 6888 (Wrigge et al. 1998) indicate that increasing the central temperature of the bubble alters the surface brightness profiles in the right direction, making them limb-brightened, though quantitative agreement with observations is still not achieved. This might indicate that heat conduction is less efficient for the large scale temperature and density structure than hitherto assumed.

Our ROSAT PSPC (Paper I) and HRI (Wrigge et al. 1998, in preparation) observations of NGC 6888 have shown that heat conduction and evaporation of clumps in a filamentary shell might play a crucial role locally for the X-ray emissivity but presently there exists no quantitative treatment on how these effects influence the energetics and dynamics of the whole bubble.

Observationally more spatially resolved X-ray observations of wind-blown bubbles with high sensitivity are needed to yield better constrains for the numerical models. To compare these models with the observations not only integral X-ray properties but also the expected X-ray morphology need to be calculated.

Acknowledgements. We would like to thank the MPE and its ROSAT team for making these observations possible. MW acknowledges many fruitful discussions with Y. H. Chu, G. García-Segura, M.-M. MacLow, U. Wessolowski, H. J. Wendker and L. Wisotzki. MW thanks Y. H. Chu for providing the optical image of S 308. MW is greatly indebted to the Institut für Astronomie und Astrophysik of the University of Kiel for hospitality during this work. Part of this work was supported by the BMBF (DARA FKZ 50 OR 9308).

References

Bohlin R.C., Savage B.D., Drake J.F., 1978, ApJ 224, 132
Chiosi C., Maeder A., 1986, ARA&A 24, 329
Chu Y.H., 1981, ApJ 249, 195
Chu Y.H., Gull, T.R., Treffers R.R., Kwitter K.B., Troland T.H., 1982, ApJ 254, 562
Chu Y.H., Treffers R.R., Kwitter K.B., 1983, ApJS 53, 937
García - Segura G., MacLow M.M., 1995a, ApJ 455, 145 (GM)
García - Segura G., MacLow M.M., 1995b, ApJ 455, 160
Hamann W.R., Schmutz W., Wessolowski U., 1988, A&A 194, 190
Hamann W.R., Koesterke L., Wessolowski U., 1993, A&A 274, 397
Heckathorn J.H., Bruhweiler F.L., Gull T.R., 1982, ApJ 252, 230
Howarth I.D., Schmutz W., 1995, A&A 294, 529
Johnson H., 1971, ApJ 167, 491
Langer N., Hamann W.-R., Lennon M., et al.,1994, A&A 290, 819
Lozinskaya T.A., 1992, Supernovae and Stellar Winds in the Interstellar Medium. American Institute of Physics, New York, N.Y.
Marston A.P., Yocum D.R., García - Segura G., Chu Y.H., 1994, ApJS 95, 151
Miller G.J., Chu Y.H., 1993, ApJS 85, 137
Pfeffermann E., Briel U.G., Hippmann H., et al., 1986, Proc. SPIE 733, 519
Plucinsky P.P., Snowden S.L., Briel U.G., Hasinger G., Pfeffermann E., 1993, ApJ 418, 519
Raymond J.C., Smith B.W., 1977, ApJS 35, 419
Schmutz W., Vacca W.D., 1991, A&AS 89, 259
Shull J.M., van Steenberg M.E., 1985, ApJ 294, 599
Snowden S.L., McCammon D., Burrows D. N., Mendenhall J. A., 1994, ApJ 424,714
Trümper J., 1983, Adv. Sp. Res. 2, 241
van der Hucht, 1992, A&AR 4, 123
van der Hucht K.A., Conti P.S., Lunström I., Stenholm B., 1981, Space Sci. Rev. 29, 227
Weaver R., McCray R., Castor J., Shapiro P., Moore R., 1977, ApJ 218, 377
Willis A.J., 1982, MNRAS 198, 897
Willis A.J., Stevens I.R., 1996, A&A 310, 577
Wrigge M., Wendker H.J., Wisotzki L., 1994, A&A 286, 219 (Paper I)
Wrigge M., Chu Y.H., Magnier E.A., Kamata Y., 1998, submitted to ApJ
Zimmermann H.U., Becker W., Belloni T., et al., 1994, EXSAS User's Guide, MPE Report 257, Garching